Quantum Electronics **33** (9) 758 – 764 (2003)

PACS numbers: 52.50.Jm; 52.70.Kz
DOI: 10.1070/QE2003v033n09ABEH002497

Dynamics of plasma production and development in gases and transparent solids irradiated by high-intensity, tightly focused picosecond laser pulses

S.V. Garnov, V.I. Konov, A.A. Malyutin, O.G. Tsar'kova, I.S. Yatskovskii, F. Dausinger

***Abstract*. The results of experimental studies of the dynamics of formation and development of a laser plasma produced in microvolumes of gases (air) and transparent solids (fused silica) by high-intensity [$I \simeq (1-2) \times 10^{14}$ W cm^{-2}], $\sim$ 22-ps, 539-nm laser pulses tightly focused in a region of diameter 4 μm are presented. The spatiotemporal distributions of the refractive index and the electron density are studied by the interferometric method with a spatial resolution of $\sim$ 1.6 μm and a temporal resolution of $\sim$ 3 ps directly during the action of excitation picosecond laser pulses. An almost complete ionisation of the initial gas was shown to occur even in the initial stage of air plasma formation, within a few picoseconds after plasma production. The irradiation of solid transparent dielectrics (fused silica) by picosecond laser pulses resulted in a reversible production of a plasma with an electron density above 10^{20} cm^{-3}, which did not cause the damage of dielectrics.**

Keywords: *laser plasma, picosecond laser pulses, interferometry, transparent dielectrics, interaction of radiation with matter.*

1. Introduction

Among the important directions of high-intensity laser radiation – matter interaction physics is the study of nonequilibrium plasmas produced in gases and condensed media by *tightly focused* (in a region a few micrometers in diameter) ultrashort laser pulses. This problem is topical both from the viewpoint of fundamental science (acquisition of new experimental data on the properties of a nonequilibrium, spatially nonuniform, high-density plasma and the mechanisms of its formation and interaction with pico- and femtosecond laser pulses) and in connection with numerous applied problems. Among the latter, we mention the development of new laser technologies for precision microprocessing of ultrastrong metals and high-temperature ceramics [1 – 6] as well as of transparent optical materials (glasses) [7 – 11], wherein the plasma produced by high-intensity ultrashort laser pulses plays a fundamental and largely decisive part.

In this work we outline the results of experimental investigations of the dynamics of the formation and development of a laser plasma generated by high-intensity ($\sim 10^{14}$ W cm^{-2}), $\sim$ 22-ps, 539-nm laser pulses in gas microvolumes and transparent solids. The main purpose of the work was precision interferometric measurements of the spatiotemporal distribution of the refractive index and the electron density of gas and solid-state plasmas directly during the action of the excitation laser pulse. For this purpose, we developed a method and built an experimental setup for the production and optical diagnostics of the laser plasma with a micrometer spatial resolution and a picosecond temporal resolution. The diagnostics involved recording 'instantaneous' interference patterns of excited material microvolumes (with more than a 100-fold magnification) using $\sim$ 3-ps probe laser pulses delayed in time [12].

Despite the fact that interference methods have long been in wide use for the investigation of laser plasmas (see, for instance, Refs [13 – 29]) and allow its spatial structure and development dynamics to be studied in principle with a high resolution, by now several basic problems remain unsolved. These problems are related, in particular, to the experimental investigation of the initial phase of plasma formation in the field of ultrashort laser pulses and to the measurement, in small volumes, of the parameters of nonuniform plasmas with a strong density gradient, which are produced upon the optical breakdown of gases and transparent solids.

2. Experimental

Fig. 1 shows the scheme of the experimental setup. A single 1078-nm, 25 – 30-ps pulse from a picosecond Nd : YAP laser with an energy of up to 5 mJ was split on a semitransparent mirror into two approximately equal parts. One of them, upon conversion to the second harmonic at 539 nm in a KDP1 crystal (the 'pump' pulse) was employed to generate plasma in the medium under study – in the air or a thin (300 μm) fused silica plate, while the other part of the beam was used to probe the plasma (the 'illumination' pulse). The use of second harmonic pulses for plasma production ensured a high contrast ratio of the pump pulses and eliminated the possible effect of the low-intensity component of the output radiation of the picosecond laser ('pedestal') on plasma formation.

S.V. Garnov, V.I. Konov, A.A. Malyutin, O.G. Tsar'kova, I.S. Yatskovskii A.M. Prokhorov General Physics Institute, Russian Academy of Sciences, ul. Vavilova 38, 119991 Moscow, Russia;
e-mail: garnov@kapella.gpi.ru;
F. Dausinger Institut fur Strahlwerkzeuge, Pfaffenwaldring 43, 70569 Stuttgart, Germany

Received 1 April 2003
Kvantovaya Elektronika **33** (9) 758 – 764 (2003)
Translated by E.N. Ragozin

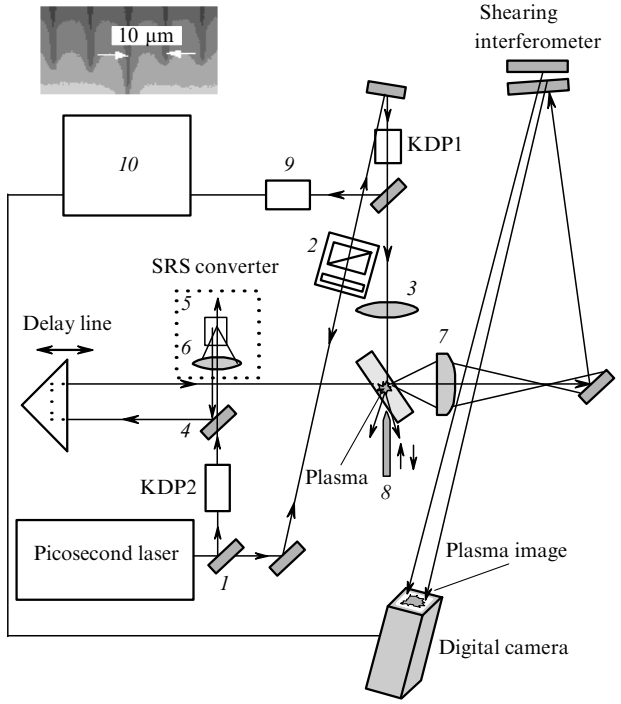

Figure 1. Scheme of the experimental setup and image of a test object (the inset): (*1*) beamsplitter ($R = 50\,\%$); (*2*) attenuator; (*3*) focusing objective ($8^{\times}$, NA = 0.2); (*4*) dichroic mirror; (*5*) cell filled with ethanol; (*6*) lens ($F = 50$ mm); (*7*) imaging objective ($20^{\times}$, NA = 0.4); (*8*) interferometric 'knife' edge; (*9*) laser pulse energy and duration meter; (*10*) system for measuring and controlling laser pulse parameters.

The excitation pulse was focused by a microobjective with the focal distance $F = 17.8$ mm ($8^{\times}$, NA = 0.2). The minimal diameter of the focused Gaussian beam was 4 μm (at a $1/e^2$ level), which was measured using an optical projection scheme intended for recording the spatial distribution of laser radiation intensity in the focal plane of the microobjective (Fig. 2).

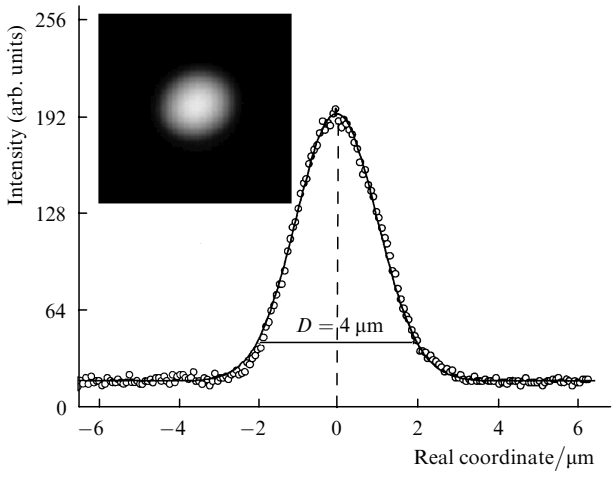

Figure 2. Spatial intensity distribution of the focused pump pulse ($\lambda_{pump} = 539$ nm, $t_{pump} \simeq 22$ ps) with a beam diameter of 4 μm ($1/e^2$) recorded with a $111^{\times}$ magnification (points – experiment, solid curve – Gaussian approximation). The inset shows the image of the excitation pulse at the target surface.

The plasma was probed by the first backward Stokes component of SRS excited by the second harmonic of the Nd : YAP laser in ethanol ($\Delta\nu = 2921$ cm^{-1}, $\lambda = 640$ nm). The SRS converter was primarily employed in order to ensure the synchronous generation of 'long' (tens of picoseconds) laser pump pulses used for plasma excitation and of the shortest possible probe radiation pulses, which provide the highest possible temporal resolution. It is known [30, 31] that the SRS of picosecond pulses in liquids should be accompanied with a significant reduction in the duration of backscattered Stokes radiation. This was confirmed in our experiments by direct measurements of the temporal SRS-radiation profile with the aid of an 'Agat' streak camera with a time resolution of ~ 2.6 ps. The pulse generated at 640 nm had a duration of 3.1 ps (Fig. 3) and an energy of up to 0.3 mJ for a second harmonic pulse duration of 22 ps and an energy conversion efficiency above 30 %.

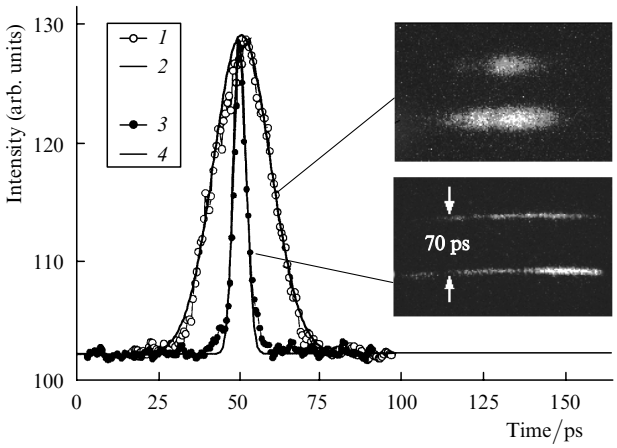

Figure 3. Pump ($\lambda_{pump} = 539$ nm, $t_{pump} \simeq 22$ ps) and probe pulse ($\lambda_{probe} = 640$ nm, $t_{probe} \simeq 3.1$ ps) intensities vs time for a sweep speed of 4.5×10^9 cm s^{-1} and a temporal resolution of 2.6 ps: (*1*, *3*) measured profiles and the corresponding images of two pairs of pulses obtained with an 'Agat' streak camera; (*2*, *4*) Gaussian pulses $\sim \exp[-4 \ln 2 (t/t_{pulse})^2]$.

The SRS converter is shown schematically in Fig. 1. The part of output laser radiation intended for the formation of illumination pulses was converted to the second harmonic in a KDP2 crystal and then focused into the quartz ethanol-filled cell by a lens with a focal length $F = 50$ mm. The backward picosecond SRS pulse was collected and collimated with the same lens, was totally reflected from a dichroic mirror (which transmitted more than 90 % of the $\lambda = 539$ nm radiation), was directed to an optical line with a variable time delay, and probed the plasma under investigation (at an angle of 90° to its axis) on transiting the delay line.

The transmitted probe radiation was 'collected' with a microobjective ($20^{\times}$, NA = 0.4), which imaged the plasma onto the matrix of a digital camera (CMOS camera, 1288×1032, Elphel Inc. [32]) with a given magnification ranging from 65 to 170. Located between the objective and the digital camera was a side shear interferometer [12, 33] made up of two plane mirrors separated by a thin ($\sim 0.2 - 0.3$ mm) air wedge with a small (no greater than 1°) wedge angle. Since the interferometer mirrors were not

parallel to each other, the reflection of the probing pulse from the front interferometer mirror ($R = 40$ %) produced the plasma shadowgraph in the matrix plane of the digital camera, while the reflection from the rear mirror ($R =$ 100 %) produced the interference plasma image. This image resulted from the interference of two spatially separated beams, the first beam fulfilling the function of the reference beam and the second one the function of the object beam [12, 29, 33]. (Because the dimensions of the plasma under study were much smaller than the probing beam diameter (~ 2 mm, $1/e^2$), the major part of the beam went past the region of induced optical inhomogeneity and did not suffer amplitude-phase distortions, i.e., could really be employed as the reference beam.) To avoid the mutual interference of subsequent (multiple) probing-beam reflections from the interferometer mirrors, an opaque screen (the so-called interferometric 'knife' edge [12]) was accommodated in the object plane (in the immediate vicinity of the plasma).

Also shown in Fig. 1 is the shadowgraph of a quartz test pattern with a line period 10 μm, which demonstrates the quality of the resultant phase microobjects and the spatial resolution achieved. When employing the imaging microobjective ($20^{\times}$, NA $= 0.4$) and the $\lambda = 640$ nm probing radiation, the limiting spatial resolution of the optical recording configuration was equal to $\lambda/\mathrm{NA} = 1.6$ μm.

3. Experimental data

3.1 Dynamics of picosecond laser-produced air plasma

Fig. 4 shows the interference patterns of laser plasma in air recorded for different probe-pulse time delays during the action of excitation picosecond pump pulses with a peak intensity (in vacuum) $I_{\mathrm{pump}} \simeq 2 \times 10^{14}$ W cm^{-2} and a duration $t_{\mathrm{pump}} \simeq 22$ ps. As in the case of plasma excitation by picosecond IR pulses ($\lambda_{\mathrm{pump}} = 1078$ nm, $t_{\mathrm{pump}} \simeq 53$ ps, $I_{\mathrm{pump}} \simeq (2 - 2.5) \times 10^{14}$ W cm^{-2} [12]), the interference patterns show the existence of three stages in laser plasma formation and development: (i) the stage of initial gas ionisation (laser-induced breakdown) and emergence of 'cold' plasma in the caustic of the focused beam (plasma 'filament', Figs 4a and 4b), which lasts for several picoseconds; (ii) the stage of efficient interaction between the plasma and laser radiation, which persists until the termination of its action and is accompanied with absorption of laser radiation, an intense heating and rapid expansion of the plasma filament (with a radial velocity of $\sim 3 \times 10^7$ cm s^{-1}) in the region facing the incident pulse (Figs 4c and 4d); and (iii) the stage of free plasma expansion with a significantly lower (by an order of magnitude) expansion velocity [12].

We paid the main attention to the initial stage of plasma formation. Our special experiments (Fig. 5) showed that plasma emerges at the leading edge of a picosecond laser pulse, when its intensity exceeds the threshold air breakdown intensity I_{th}. In particular, for a given peak pump pulse intensity $I_{\mathrm{pump}} \simeq 2 \times 10^{14}$ W cm^{-2}, the instant of plasma emergence is 16 – 18 ps ahead of the peak of the pulse. As the peak intensity (energy) of the excitation pulse is lowered, the instant of plasma emergence shifts gradually towards its maximum to coincide with it on reaching the threshold of laser-induced air breakdown ($I_{\mathrm{pump}} \simeq I_{\mathrm{th}} \simeq 2.5 \times 10^{13}$ W cm^{-2}). [The above threshold intensity value was measured in two independent ways in our experiments: visually (from the spark production) and from the occurrence of some kind of interference fringe distortions in the interference patterns recorded. In this case, both methods of breakdown threshold evaluation yielded the same results.]

The experimental data shown in Fig. 5 demonstrate clearly that not only the instant of plasma appearance, but also the initial plasma dimensions (in particular, the plasma filament diameter) are determined primarily by the dimensions of the spatial region wherein the laser radiation intensity $I(x, y, z, t)$ exceeds the threshold of laser-induced air breakdown: $I(x, y, z, t) \geqslant I_{\mathrm{th}}$. Indeed, the interference

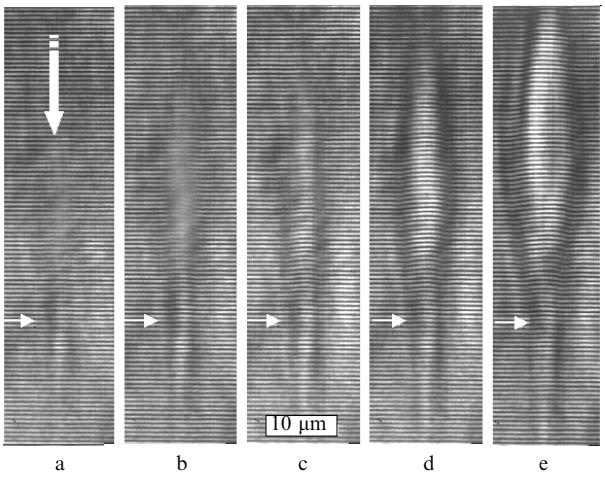

Figure 4. Dynamics of the development of a picosecond laser plasma produced in air for a probe pulse delay of 3.34 (a), 6.7 (b), 10 (c), 16.7 (d), and 27 ps (e). The zero delay corresponds to the instant of plasma initiation. The pump pulse ($\lambda = 539$ nm, $t_{\mathrm{pump}} \simeq 22$ ps, $I \simeq 2 \times 10^{14}$ W cm^{-2}) is aligned with the vertical line (downwards). The horizontal arrows indicate the focus position. The plasma production threshold (the air breakdown) is $I_{\mathrm{th}} \simeq 2.5 \times 10^{13}$ W cm^{-2}.

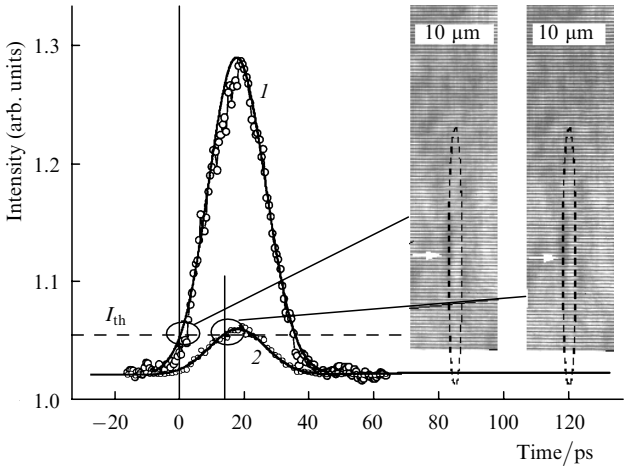

Figure 5. Initial formation stage of laser plasma produced in air ($\lambda = 539$ nm, $t_{\mathrm{pump}} \simeq 22$ ps) for a pulse with a peak intensity of 2×10^{14} (*1*) and 3.3×10^{13} W cm^{-2} (*2*), close to the threshold air breakdown intensity ($I_{\mathrm{th}} \simeq 2.5 \times 10^{13}$ W cm^{-2}). The plasma emerges when the pulse reaches the breakdown threshold, the plasma filament diameter is determined by the dimensions of the regions where $I_{\mathrm{th}} \leqslant I(x, y, z, t)$ (marked out with contour lines in the corresponding interference patterns obtained at the points in time 3.38 and 16.7 ps).

patterns (Fig. 5) of the initial plasma formation stage recorded with laser pulses with peak intensities differing by nearly an order of magnitude – $I_{\rm pump} \simeq 2 \times 10^{14}$ W cm^{-2} (a time delay of 3.38 ps) and $I_{\rm pump} \simeq 3.5 \times 10^{13}$ W cm^{-2} (a time delay of 16.7 ps) – are hardly different, and the dimensions of ionised gas domain corresponding to the points in time 3.38 and 16.7 ps virtually coincide with the dimensions of the domain bounded by the threshold intensity, which is indicated with contour lines of equal (threshold) intensity in the interference patterns. The influence of radiation self-trapping (self-focusing), typical for the plasma formation under femtosecond pulse irradiation, was discovered at none of the development stages of the plasma produced upon irradiation by 22-ps laser pulses.

The resultant interferometric plasma images enable not only a detailed study of plasma shape and development dynamics, but also a determination of the spatiotemporal distributions of density and refractive index. An analysis of the interference patterns given in Fig. 4 (of the direction and shifts of interference fringes) testifies to a significant reduction of the refractive index of the ionised material in comparison with the ambient unperturbed air, which results from the 'negative' free-electron contribution to the plasma refractive index. To exemplify, Fig. 6 shows the radial profiles of the refractive index $n(r)$ and electron density $N_{\rm e}(t)$ of the plasma near the focal plane reconstructed from the interference pattern of Fig. 4d through the conventional procedure of inverse Abelian transformation [12, 29, 34]:

$$n(r) = n_0 - \frac{\lambda}{\pi}\int_{r^2}^{R^2} \left.\frac{{\rm d}\Delta(r)}{{\rm d}r}\right|_{r=\sqrt{u}} \frac{1}{2\sqrt{u}}\,\frac{1}{(u-r^2)^{1/2}}\,{\rm d}u\,,$$
$$\Delta(r) = \frac{2}{\lambda}\int_r^R \frac{(n(x)-n_0)x{\rm d}x}{(x^2-r^2)^{1/2}}, \qquad (1)$$

where $\Delta(r)$ is the experimentally measured interference fringe shift as a function of the radial coordinate r [corresponds to a probe-wave phase shift $\Delta\Phi(r) = 2\pi\Delta(r)$]; R is the radius of the plasma volume; n_0 is the refractive index of the environment ($n_0 \simeq 1.000278$ for air under normal conditions).

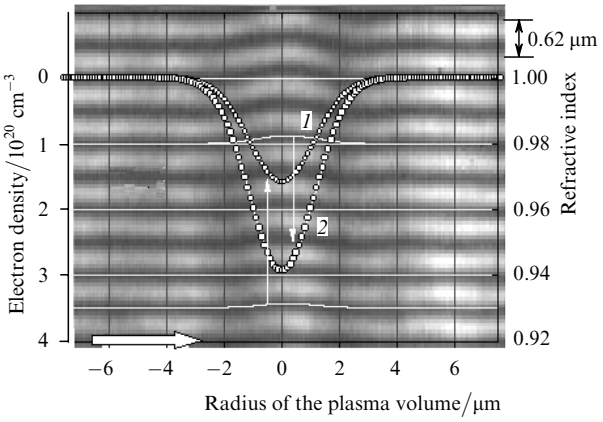

Figure 6. Radial distributions of the electron density and refractive index in the air plasma in the focal region (indicated with a horizontal arrow) for $N_{\rm e}^{\rm max} = 1.6 \times 10^{20}$ (*1*) and 3×10^{20} cm^{-3} (*2*). The pump pulse ($\lambda = 539$ nm, $t_{\rm pump} \simeq 22$ ps, $I \simeq 2 \times 10^{14}$ W cm^{-2}) travels downwards. The probing-pulse time delay is 16.7 ps (see Fig. 4d).

The electron plasma density $N_{\rm e}(t)$ was determined from the dependence $n(r)$ using the Drude model for the free-electron contribution to the refractive index [34, 35]:

$$n(t) = \left[n_0^2 - \left(\frac{\omega_{\rm p}(t)}{\omega}\right)^2\right]^{1/2}, \quad \omega_{\rm p}^2(t) = \frac{N_{\rm e}(t)e^2}{\varepsilon_0 m_{\rm e}}, \qquad (2)$$

where $\omega = 2.94 \times 10^{15}$ rad s^{-1} is the angular frequency of the probing radiation ($\lambda_{\rm probe} = 640$ nm); $\omega_{\rm p}(t)$ is the plasma frequency; e and $m_{\rm e}$ are the electron charge and mass; and ε_0 is the dielectric constant. In this case, owing to the smallness of $\omega_{\rm p}/\omega$ the profile of electron density actually reproduces the profile of refractive index, while the ion contribution to the refractive index of a high-density plasma, as usual, can be neglected [34].

A significant result of our work is the fact of recording extremely large values of electron plasma density in our experiments, which range up to $\sim 3 \times 10^{20}$ cm^{-3} (Fig. 6) and are indicative of a practically complete air ionisation by picosecond laser pulses. (Recall that the maximal attainable electron density in the fully ionised air at normal conditions is $\sim 3.6 \times 10^{20}$ cm^{-3}. In this case, the plasma remains transparent at both the exciting and probing radiation wavelengths, for which the critical electron density is higher by an order of magnitude: 3.8×10^{21} and 2.7×10^{21} cm^{-3}, respectively.) So high an electron density becomes observable at the centre of the plasma filament – near the focal plane – even early in the plasma formation, only a few picoseconds after plasma emergence (see Fig. 4b), to attain its peak value in the region of a rapidly expanding plasma (Fig. 7) at the peak intensity of the laser pulse. We note that quite high (above 10^{20} cm^{-3}) free-electron densities persist in the plasma for a considerable time period (hundreds of picoseconds [12]), and it is not until several nanoseconds after their appearance that the electron density gradually decays to 10^{19} cm^{-3} and lower [29].

3.2 Dynamics of picosecond laser plasma produced in fused silica

Another object investigated in our work was the nonequilibrium solid-state plasma induced by high-intensity picosecond laser pulses in the volume of transparent solids (fused silica). To study the dynamics of its formation and development, we used the same experimental setup and technique for recording interferometric images of the interaction region. Unlike air, along with the occurrence of a nonequilibrium plasma (with mainly the electron component) in the volume of fused silica we also recorded other laser-induced processes and effects which were responsible for the spatiotemporal modulation of the refractive index of the medium, including the nonlinear-optical Kerr effect as well as different manifestations of the structural modification of the source material related to the production of radiation-induced defects. Consideration of the entire range of effects under study goes beyond the scope of our paper, and we dwell at some length on one of the most interesting experimental results – the discovery of the reversible (not resulting in the subsequent laser-induced material damage) production of nonequilibrium electrons with a density exceeding 10^{20} cm^{-3} in the volume of transparent solids irradiated by picosecond laser pulses. So high a 'nondestructive' density of a nonequilibrium solid-state plasma in transparent dielectrics was previously recorded only with femtosecond ($\sim 100 - 150$ fs) laser

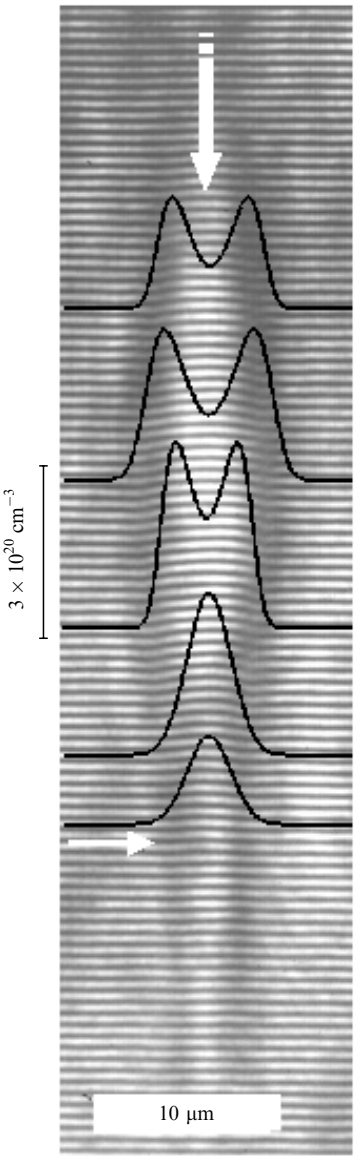

Figure 7. Radial-axial distribution of the electron density in the air plasma for a probe–pulse time delay of 16.7 ps (see Fig. 4d). The horizontal arrow indicates the focus position. The pump pulse is aligned with the vertical arrow (downwards).

pulse irradiation [36, 37], and it was believed that the application of longer pulses, picosecond in particular, should undoubtedly result in material destruction.

Fig. 8 shows the interference patterns of the interaction region of a sample of fused silica, which were obtained during the action of a sharply focused high-intensity ($I_{\text{pump}} \simeq 1.2 \times 10^{14}$ W cm^{-2}) picosecond laser pulse (for a probing-pulse delay of ~ 10 ps) and a long period of time after its termination. Since the peak intensity of the pump pulse is rather high [in particular, it is many times the threshold intensity of optical damage for fused silica $I_{\text{th}} \simeq (1.2 - 1.5) \times 10^{12}$ W cm^{-2}], in the volume of the sample there appears a domain of significant size that clearly exhibits a shift of interference fringes caused by changes of the refractive index of the medium (Fig. 8a).

The magnitude of interference fringe shifts and, what is most important, the shift direction vary significantly along

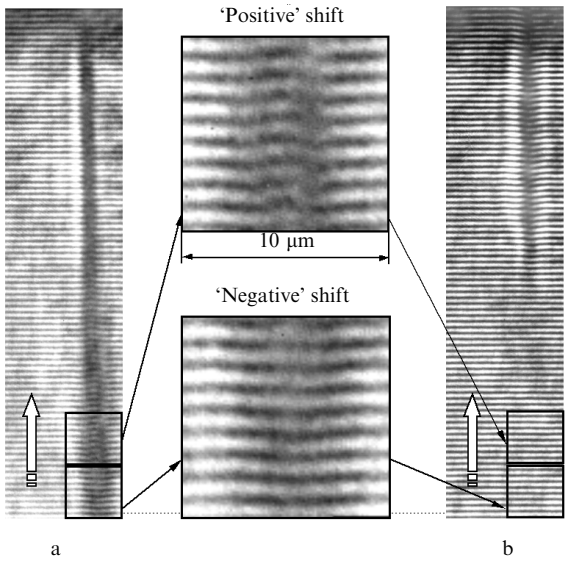

Figure 8. Interference patterns of the region of interaction between a picosecond laser pulse and fused silica recorded for a time delay of 10 ps (a) and ~ 1 s (b). During the action of the pulse, 'positive' and 'negative' interference fringe shifts are recorded in the framed regions. The pump pulse ($I_{\text{pump}} \simeq 1.2 \times 10^{14}$ W cm^{-2}, $\lambda_{\text{pump}} = 539$ nm, $t_{\text{pump}} \simeq 22$ ps) is aligned with the arrow (upwards). The optical damage threshold for fused silica is $I_{\text{th}} \simeq (1.2 - 1.5) \times 10^{12}$ W cm^{-2} and the sample thickness is 300 μm.

the beam axis, depending on its position and the distance to the focal plane. This is related to the manifestation of physical processes and the mechanisms of induced refractive index formation that are different in nature. In particular, the 'positive' fringe shift observed in the major part of the interaction region is supposedly caused by the Kerr nonlinearity of the medium and the radiation-induced defects produced (self-trapped excitons), which make a positive contribution to the induced refractive index in silica. The 'negative' shift results from the generation of nonequilibrium electrons, which decrease the refractive index [36, 37].

In the vicinity of the focus, the observed changes of refractive index are irreversible in nature, which is related to the laser-induced structural change of fused silica and optical damage to the material, which shows up clearly in the upper part of the interference pattern in Fig. 8b. However, away from the focus, where the laser radiation intensity is moderate, the variations of refractive index prove to be completely reversible, i.e., the optical properties of quartz are hardly changed after laser irradiation (Fig. 8b). This circumstance allows, in particular, a conclusion that the nonequilibrium electrons with a density of $\sim 3 \times 10^{20}$ cm^{-3} observed during laser irradiation (Fig. 9) by themselves do not cause laser-induced damage to the material. The electron density of the solid-state plasma and the induced refractive index were determined through the procedure of inverse Abelian transformation outlined above.

4. Interferometry of small bulk phase objects

Since the accuracy of reconstruction of the spatial distribution of refractive index and hence the electron plasma density may largely depend on the amplitude-phase

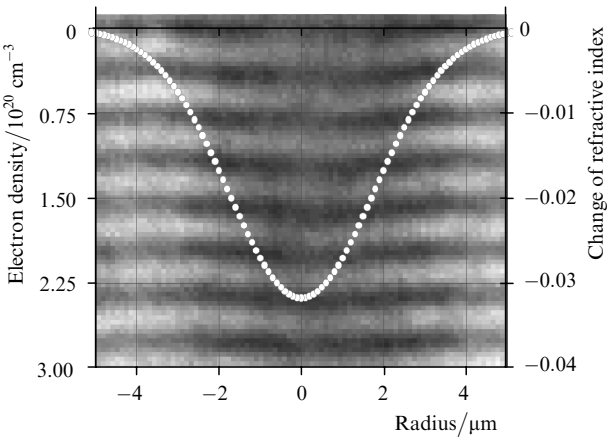

Figure 9. Radial distribution of the change of refractive index [$\Delta n = n(r) - n_0$, $n_0 = 1.4575$] and the density of nonequilibrium electrons in fused silica. The time delay of the probing pulse is 10 ps (see Fig. 8a).

distortions introduced by the imaging optical system [12, 29], we investigated the effect of parameters of the optical elements (including aberrations, magnification, numerical aperture of the imaging objective, and its spatial resolution) on image formation and its correspondence to the phase object under investigation. To this end, an algorithm was elaborated and computer modelling was made of the interferometric image formation of small bulk phase objects with the use of the FRESNEL code [12, 29, 38].

Fig. 10 shows the results of numerical modelling performed for an axially symmetric phase object with parameters corresponding to a 40-μm long plasma filament 4 μm in diameter and a phase incursion of $0.35\lambda_{\text{probe}}$. The calculations were performed with the inclusion of real parameters of the experimental setup – the probe radiation wavelength, the magnification, the numerical aperture, and the spatial resolution. As follows from the results outlined, the plasma-imaging configuration (with a $20^{\times}$ imaging microobjective, NA = 0.4) employed in our experiments ensures a perfect fit of the initial ('undistorted') interference pattern of the object (Fig. 10a) to its magnified (recorded) image (Fig. 10b). The distortions related to the objective aperture finiteness begin to show up only when employing optics with a smaller numerical aperture – NA = 0.2 and 0.11 (Figs 10c and 10d). Therefore, in our experiments we have reached a sufficiently high precision of the reconstruction of plasma parameters and, in particular, the spatial profile of the refractive index.

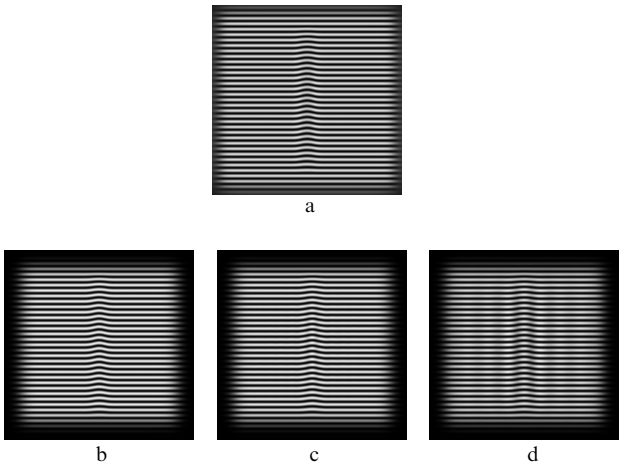

Figure 10. Results of computer simulation of the formation of interferometric images ($\lambda_{\text{probe}} = 640$ nm) of small bulk phase objects – initial interference pattern of an axially symmetric phase object measuring 4×40 μm in the object plane (a) and its magnified ($65^{\times}$) images (b – d) for NA = 0.4 (b), 0.2 (c), and 0.11 (d). The phase incursion is $0.35\lambda_{\text{probe}}$.

5. Conclusions

Our experiments have demonstrated that even early in the air plasma formation, within a few picoseconds after its emergence, there occurs a practically complete ionisation of the initial gas and the electron plasma density rises to $\sim 3 \times 10^{20}$ cm^{-3}. In the volume of solid transparent dielectrics (fused silica), under the action of picosecond laser pulses there occurs a reversible plasma production with an electron density above 10^{20} cm^{-3}.

The system employed in our experiments for recording interferometric images of the plasma was shown to provide a faithful reproduction of its shape and the spatial distribution of refractive index.

On the basis of highly efficient (with an efficiency of more than 30 %) successive conversion of picosecond Nd : YAP-laser pulses to the second harmonic and the first Stokes component of backward stimulated Raman scattering in ethanol, we have experimentally realised the synchronous generation of laser pulses with durations of 3 ps ($\lambda = 640$ nm) and 22 ps ($\lambda = 539$ nm).

Acknowledgements. This work was supported by the Russian Foundation for Basic Research (Grant Nos 2-02-17718 and 03-02-16725) and the PRIMUS Project (Grant No. 13N771016).

References

1. Kononenko T.V., Garnov S.V., Klimentov S.M., Konov V.I., Loubnin E.N., Dausinger F., Raiber A., Taut C. *Appl. Surf. Science*, **109 – 110**, 48 (1997).
2. Garnov S.V., Klimentov S.M., Konov V.I., Kononenko T.B., Dausinger F. *Kvantovaya Elektron.*, **25** (1), 45 (1998) [*Quantum Electron.*, **28** (1), 42 (1998)].
3. Dausinger F., Abeln T., Breitling D., Radtke J., Konov V., Garnov S., Klimentov S., Kononenko T., Tsarkova O. *Laser Opto*, **31** (3), 78 (1999).
4. Kononenko T.B., Konov V.I., Garnov S.V., Danielius R., Piskarskas A., Tamoshkauskas G., Dausinger F. *Kvantovaya Elektron.*, **28** (2), 167 (1999) [*Quantum Electron.*, **29** (8), 724 (1999)].
5. Klimentov S.M., Kononenko T.B., Pivovarov P.A., Garnov S.V., Konov V.I., Prokhorov A.M., Breitling D., Dausinger F. *Kvantovaya Elektron.*, 31 (5), 378 (2001) [*Quantum Electron.*, **31** (5), 378 (2001)].
6. Kononenko T.V., Konov V.I., Garnov S.V., Klimentov S.M., Dausinger F. *Laser Phys.*, **11** (3), 343 (2001).
7. Glezer E.N., Milosavljevic M., Huang L., Finlay R.J., Her T.-H., Callan J.P., Mazur E. *Opt. Lett.*, **24**, 2023 (1996).
8. Schaffer C.B., Brodeur A., Garcia J.F., Mazur E. *Opt. Lett.*, **26**, 93 (2001).
9. Schaffer C.B., Garcia J.F., Mazur E. *Appl. Phys. A*, **76**, 351 (2003).
10. Marcinkevicius A., Juodkazis S., Watanabe M., Miwa M., Matsuo S., Misawa H., Nishii J. *Opt. Lett.*, **26**, 277 (2001).

11. Li Y., Itoh K., Watanabe W., Yamada K., Kuroda D., Nishii J., Jiang Y. *Opt. Lett.*, **26**, 1912 (2001).
12. Garnov S.V., Konov V.I., Malyutin A.A., Tsarkova O.G., Yatskovsky I.S., Dausinger F. *Laser Phys.*, **13** (3), 386 (2003).
13. Belland P., De Michelis C., Mattioli M. *Opt. Commun.*, **3**, 7 (1971).
14. Attwood D.T., Coleman L.W. *Appl. Phys. Lett.*, **24**, 408 (1974).
15. Azechi H., Oda S., Tanaka K., Norimatsu T., Sasaki T., Yamanaka T., Yamanaka C. *Phys. Rev. Lett.*, **39**, 1144 (1977).
16. Attwood D.T., Sweeney D.W., Auerbach J.M., Lee P.H.Y. *Phys. Rev. Lett.*, **40**, 184 (1978).
17. Attwood D.T. *IEEE J. Quantum Electron.*, **14** (12), 909 (1978).
18. Raven A., Willi O. *Phys. Rev. Lett.*, **43**, 278 (1979).
19. Vlasov N.G., Korchazhkin S.V., Matsonashvili R.B., Petryakov V.M., Sobolev S.S., Chalkin S.F. *Opt. Spektrosk.*, **59** (4), 934 (1985).
20. Da Silva L.B., Barbee T.W., Cauble Jr. R., Celliers P., Ciarlo D., Libby S., London R.A., Matthews D., Mrowka S., Moreno J.C., Ress D., Trebes J.E., Wan A.S., Weber F. *Phys. Rev. Lett.*, **74**, 3991 (1995).
21. Shao Y.L., Ditmire T., Tisch J.W.G., Springate E., Marangos J.P., Hutchinson M.H.R. *Phys. Rev. Lett.*, **77**, 3343 (1996).
22. Sarkisov G.S., Bychenkov V.Yu., Novikov V.N., Tikhonchuk V.T., Maksimchuk A., Chen S.-Y., Wagner R., Mourou G., Umstadter D. *Pis'ma Zh. Eksp. Teor. Fiz.*, **66** (12), 787 (1997).
23. Ditmire T., Gumbrell E.T., Smith R.A., Djaoui A., Hutchinson M.H.R. *Phys. Rev. Lett.*, **80** (4), 720 (1998).
24. Breitling D., Schittenhelm H., Berger P., Dausinger F., Hugel H. *Appl. Phys. A*, **69**, S505 (1999).
25. Sarkisov G.S., Bychenkov V.Yu., Novikov V.N., Tikhonchuk V.T., Maksimchuk A., Chen S.-Y., Wagner R., Mourou G., Umstadter D. *Phys. Rev. E*, **59**, 7042 (1999).
26. Edwards M.J., MacKinnon A.J., Zweiback J., Shigemori K., Ryutov D., Rubenchik A.M., Keilty K.A., Liang E., Remington B.A., Ditmire T. *Phys. Rev. Lett.*, **87**, 085004 (2001).
27. Couairon A., Berge L. *Phys. Rev. Lett.*, **88**, 135003-1 (2002).
28. Smith R.F., Dunn J., Nilsen J., Shlyaptsev V.N., Moon S., Filevich J., Rocca J.J., Marconi M.C., Hunter J.R., Barbee T.W. *Phys. Rev. Lett.*, **89**, 065004 (2002).
29. Garnov S.V., Malyutin A.A., Tsarkova O.G., Konov V.I., Dausinger F. *Proc. SPIE Int. Soc. Opt. Eng.*, **4637**, 31 (2002).
30. Chevalier R., Sokolovskaia A., Tcherniega N., Rivoire G. *Opt. Commun.*, **82**, 117 (1991).
31. Tcherniega N., Sokolovskaia A., Kudriavtseva A.D., Barille R., Rivoire G. *Opt. Commun.*, **181**, 197 (2000).
32. www.elphel.com.
33. Sarkisov G.S. *Prib. Tekh. Eksp.*, (5), 110 (1996).
34. Fortov V.E. (Ed.) *Entsiklopediya nizkotemperaturnoi plazmy* (Encyclopaedia of Low-Temperature Plasma) (Moscow: Nauka, 2000).
35. Born M., Wolf E. *Principles of Optics* (Cambridge: University Press, 1999).
36. Martin P., Guizard S., Daguzan Ph., Petite G., Oliveira P.D., Meynadier P., Perdrix M. *Phys. Rev. B*, **55** (9), 5799 (1997).
37. Quere F., Guizard S., Martin P., Petite G., Gobert O., Meynadier P., Perdrix M. *Appl. Phys. B*, **68**, 459 (1999).
38. Epatko I.V., Malyutin A.A., Serov R.V., Solov'ev D.A., Chulkin A.D. *Kvantovaya Elektron.*, **25** (8), 717 (1998) [*Quantum Electron.*, **28** (8), 697 (1998)].